
mLaSDI: Multi-stage latent space dynamics identification

William Anderson

Center for Applied Scientific Computing
Lawrence Livermore National Laboratory
Livermore, CA 94550
anderson316@llnl.gov

Seung Whan Chung

Center for Applied Scientific Computing
Lawrence Livermore National Laboratory
Livermore, CA 94550
chung28@llnl.gov

Youngsoo Choi

Center for Applied Scientific Computing
Lawrence Livermore National Laboratory
Livermore, CA 94550
choi15@llnl.gov

Abstract

Determining accurate numerical solutions of partial differential equations (PDEs) is an important task in many scientific disciplines. However, solvers can be computationally expensive, leading to the development of reduced-order models (ROMs). Recently, Latent Space Dynamics Identification (LaSDI) was proposed as a data-driven, non-intrusive ROM framework. LaSDI compresses the training data using an autoencoder and learns a system of user-chosen ordinary differential equations (ODEs), which govern the latent space dynamics. This allows for rapid predictions by interpolating and evolving the low-dimensional ODEs in the latent space. While LaSDI has produced effective ROMs for numerous problems, the autoencoder can have difficulty accurately reconstructing training data while also satisfying the imposed dynamics in the latent space, particularly in complex or high-frequency regimes. To address this, we propose multi-stage Latent Space Dynamics Identification (mLaSDI). With mLaSDI, several autoencoders are trained sequentially in stages, where each autoencoder learns to correct the error of the previous stages. We find that applying mLaSDI with small autoencoders results in lower prediction and reconstruction errors, while also reducing training time compared to LaSDI.

1 Introduction

Advances in computational power and numerical techniques help to facilitate increasingly accurate and complex simulations of time-dependent partial differential equations (PDEs). High-fidelity numerical simulations improve understanding in many scientific fields such as engineering [9, 12, 23], physics [35, 37] and biology [27]. While accurate, these simulations are often computationally expensive, which necessitates the use of reduced-order models. In this work, we focus on PDEs with parametric dependencies that influence the initial conditions or underlying physics.

There exists rich theory for projection-based reduced-order models, where the governing equations are known [3, 5]. Yet, linear projection-based approaches such as the proper orthogonal decomposition struggle with advection-dominated problems [29, 33]. Nonlinear projection techniques have shown improved accuracy for these problems [7, 13, 24]. Regardless, projection-based approaches are often intrusive and require knowledge of the governing equations.

Another approach is to use non-intrusive reduced-order models, which are purely data-driven. These approaches develop ROMs without any knowledge of the underlying PDE. However, many non-intrusive approaches lack interpretability, which makes generalizing results beyond the training data difficult. This is the main motivation for the reduced-order modeling framework introduced by Fries et al. [14], Latent Space Dynamics Identification (LaSDI). LaSDI trains an autoencoder which learns interpretable dynamics of the compressed data by applying Sparse Identification of Nonlinear Dynamics (SINDy) [8] in the latent space. LaSDI uses SINDy to learn ODEs for every input parameter in the training data, and then interpolates these ODEs for an unseen training parameter. Since its inception, there have been several improvements and variations to the LaSDI algorithm. For example, developments include simultaneous training of the autoencoder and SINDy with residual-based active learning [16], the introduction of Gaussian Processes (GPs) to interpolate for SINDy coefficients [6], implementations the weak form of SINDy to deal with noisy data [17, 36], and implementing physical constraints in the latent space [28]. While LaSDI and its variants have been successfully applied to a wide range of problems, there remains significant room for improvement. In particular, LaSDI often requires autoencoders to balance accurate data reconstruction with enforcing prescribed latent dynamics, an inherently conflicting objective. This compromise can lead to poor reconstructions and inaccurate predictions for unseen parameters. Additionally, training these models can be computationally expensive, often requiring large autoencoders and extensive hyperparameter tuning to achieve acceptable performance.

To overcome these limitations, we introduce **multistage Latent Space Dynamics Identification (mLaSDI)**, a general framework that extends any variant of LaSDI by training multiple autoencoders sequentially. Each stage learns to reconstruct the residual left by earlier stages while simultaneously identifying new latent dynamics. This allows us to dramatically improve reconstruction and prediction accuracy, often reducing error by an order of magnitude, with less need for large autoencoders or extensive hyperparameter tuning. Source code for this project is based on GPLaSDI: <https://github.com/LLNL/GPLaSDI>.

Related Works. Several works have applied equation-learning algorithms [8, 34] to approximate the underlying latent space dynamics [4, 11, 21, 31]. Perhaps the most closely related work to LaSDI is that of Champion et al. [10], where an autoencoder is trained to learn a SINDy representation in the latent space. However, their proposed method is not parameterized and is less generalizable than the LaSDI framework.

Multiple authors have also proposed the idea of training sequential neural networks to achieve increased accuracy. Both [1] and [39] introduce multi-stage neural networks, where each stage a new network is introduced to learn the error from the previous stages. In [39] the initial weights of the networks are altered in order to learn the residual more quickly, while [1] increases the network size at each stage. Focusing specifically on physics-informed neural networks, [19] introduces multiple stages of networks, where each stage involves simultaneously training a linear and nonlinear network to increase accuracy. Several authors [38, 40, 41] have also explored the use of stacked autoencoders to increase reconstruction accuracy.

To our knowledge, mLaSDI is the first multi-stage architecture designed for interpretable latent dynamics, where each stage must respect dynamical constraints. This is a notable departure from previous residual-learning networks and a fundamentally different challenge compared to prior stacked architectures. We demonstrate its performance on several PDE benchmark problems, showing that mLaSDI outperforms traditional LaSDI variants both in accuracy and computational efficiency.

2 LaSDI Framework

Before discussing mLaSDI, we must briefly describe the LaSDI algorithm. Although mLaSDI is applicable to any LaSDI variant, we choose to focus on Gaussian-Process based LaSDI (GPLaSDI). We briefly summarize GPLaSDI and refer the reader to [6] for further details.

2.1 Governing Equations

We consider ODEs of the form

$$\frac{d}{dt}\mathbf{u}(t;\boldsymbol{\mu}) = \mathbf{f}(\mathbf{u}), \quad \mathbf{u}(0;\boldsymbol{\mu}) = \mathbf{u}_0(\boldsymbol{\mu}), \quad (1)$$

where $\mathbf{u} : \mathbb{R}^+ \rightarrow \mathbb{R}^{N_u}$ is the state vector, $f : \mathbb{R}^{N_u} \rightarrow \mathbb{R}^{N_u}$ is a vector-valued function, and $\boldsymbol{\mu} \in \mathcal{D} \subset \mathbb{R}^N$ is an input parameter. This parameter may affect either the physics of the simulation or the initial condition. Our dynamical system 1 often arises from the spatial discretization of a PDE, although this need not be the case.

We assume no knowledge of the underlying dynamical system, and only consider snapshots of the state vector \mathbf{u} at times t_i , $i = 0, 1, \dots, N_t$. For simplicity, we assume uniform timestep size $\Delta t = t_{i+1} - t_i$. Given an input parameter $\boldsymbol{\mu}^{(i)}$, we form snapshots of the state vector into the training data matrix $U^{(i)} = [\mathbf{u}^{(i)}(0), \mathbf{u}^{(i)}(t_1), \dots, \mathbf{u}^{(i)}(N_t)] \in \mathbb{R}^{(N_u \times N_t)}$. Concatenating the snapshots from each of our N_μ training parameters, we obtain the tensor

$$\mathbf{U} = [U^{(1)}, U^{(2)}, \dots, U^{(N_\mu)}] \in \mathbb{R}^{N_\mu \times (N_t+1) \times N_u}, \quad (2)$$

where \mathbf{U} is our training data tensor.

2.2 Data compression

Often the state dimension N_u is large, and so we compress the data to facilitate easier analysis and modeling. For this manuscript, we always compress the training data \mathbf{U} with an autoencoder [18]. These autoencoders consist of an encoder map which compresses the data, and a decoder map which attempts to reconstruct the data. More precisely, the encoder learns a map $\mathcal{G}_{\text{enc}} : \mathbb{R}^{N_u} \rightarrow \mathbb{R}^{N_z}$ and the decoder learns the map $\mathcal{G}_{\text{dec}} : \mathbb{R}^{N_z} \rightarrow \mathbb{R}^{N_u}$, where $N_z \ll N_u$. These mappings allow us to compress snapshots of the state vector $\mathbf{u}^{(i)}(t_k) \in N_u$ to low-dimensional latent variables $\mathbf{z}^{(i)}(t_k) \in N_z$ given by $\mathbf{z}^{(i)}(t_k) := \mathcal{G}_{\text{enc}} \mathbf{u}^{(i)}(t_k)$. We can similarly map the training data matrix $U^{(i)}$ to the low dimensional compressed training data matrix $Z^{(i)} = [\mathbf{z}^{(i)}(0), \mathbf{z}^{(i)}(t_1), \dots, \mathbf{z}^{(i)}(N_t)]$. The compressed data tensor from our N_μ training data simulations is then given by

$$\mathbf{Z} = [Z^{(1)}, Z^{(2)}, \dots, Z^{(N_\mu)}] \in \mathbb{R}^{N_\mu \times (N_t+1) \times N_z}. \quad (3)$$

We also define the autoencoder reconstruction of our training data tensor $\hat{\mathbf{U}}$, given by

$$\hat{\mathbf{U}} := \mathcal{G}_{\text{dec}} \mathcal{G}_{\text{enc}} \mathbf{U}. \quad (4)$$

Our autoencoder attempts to minimize the reconstruction loss

$$\mathcal{L}_{\text{AE}}(\boldsymbol{\theta}_{\text{enc}}, \boldsymbol{\theta}_{\text{dec}}) = \|\mathbf{U} - \hat{\mathbf{U}}\|^2, \quad (5)$$

where $\|\cdot\|$ is the element-wise ℓ^2 -norm.

2.3 Latent Space Dynamics Identification

Autoencoders allow us to compress the training data, but they do not provide any interpretability in the latent space. To address this, we impose user-chosen dynamics in the latent space which the autoencoder attempts to satisfy. Applying SINDy [8], we approximate the time derivative of our compressed snapshots with a library of functions satisfying

$$\dot{Z}^{(i)} \approx \hat{Z}^{(i)} := \Theta(Z^{(i)}) \Xi^{(i)}, \quad (6)$$

where $\Theta(Z^{(i)})$ is a user-chosen library of functions and $\Xi^{(i)}$ is a matrix of coefficients we must solve for. While we are free to choose any terms in our library, a common choice for LaSDI variants is to assume linear dynamics [6, 16] so that the library and coefficients are given by

$$\Theta(Z^{(i)}) = (\mathbf{1} (Z^{(i)})^\top), \quad \Xi^{(i)} = (\mathbf{b}^{(i)} A^{(i)})^\top, \quad (7)$$

where $\mathbf{1} \in \mathbb{R}^{N_t}$ is a vector with all entries equal to 1, $\mathbf{b}^{(i)} \in \mathbb{R}^{N_z}$, and $A^{(i)} \in \mathbb{R}^{N_z \times N_z}$. We will also assume linear dynamics for all LaSDI examples described in this paper. To determine the coefficients $\Xi^{(i)}$, we solve the least squares problem

$$\min_{\mathbf{b}^{(i)} \in \mathbb{R}^{N_z}, A^{(i)} \in \mathbb{R}^{N_z \times N_z}} \|\hat{Z}^{(i)} - (\mathbf{1} (Z^{(i)})^\top) (\mathbf{b}^{(i)} A^{(i)})^\top\|^2. \quad (8)$$

While many applications of SINDy enforce sparsity in the coefficient matrix (as the algorithm's name implies), we use a dense coefficient matrix. This allows us to have greater representation power in

the latent space. Additionally, if we enforced sparsity, the SINDy coefficients corresponding to each training parameter would have a different sparsity pattern. This sparsity would then be violated when interpolating for unseen parameter values, as we will see in Section 2.4.

After solving the least squares problem (8) for each of our N_μ simulations, we form tensors for our SINDy approximations of the latent space dynamics and the corresponding coefficient matrices

$$\dot{\mathbf{Z}} = [\dot{\mathbf{Z}}^{(1)} \ \dot{\mathbf{Z}}^{(2)} \ \dots \ \dot{\mathbf{Z}}^{(N_\mu)}] \in \mathbb{R}^{N_\mu \times (N_t+1) \times N_z} \quad (9)$$

$$\Xi = [\Xi^{(1)} \ \Xi^{(2)} \ \dots \ \Xi^{(N_\mu)}] \in \mathbb{R}^{N_\mu \times N_z \times (N_z+1)}. \quad (10)$$

We can now define our dynamics identification loss

$$\mathcal{L}_{\text{DI}}(\Xi) = \|\dot{\mathbf{Z}} - \dot{\mathbf{Z}}\|^2. \quad (11)$$

Additionally, we penalize the norm of our SINDy coefficients to obtain the loss function for GPLaSDI

$$\mathcal{L}(\boldsymbol{\theta}_{\text{enc}}, \boldsymbol{\theta}_{\text{dec}}, \Xi) = \mathcal{L}_{\text{AE}}(\boldsymbol{\theta}_{\text{enc}}, \boldsymbol{\theta}_{\text{dec}}) + \beta_1 \mathcal{L}_{\text{DI}}(\Xi) + \beta_2 \|\Xi\|^2 \quad (12)$$

By training autoencoders with the loss function (12), our autoencoder attempts to accurately reconstruct the training data while satisfying linear dynamics in the latent space.

2.4 Gaussian-Process Interpolation

The last component of GPLaSDI is interpolating SINDy coefficients from our training data for a general input parameter value $\boldsymbol{\mu}^{(*)}$. For full details we refer to [6]. In short, we fit a separate GP [32] to each of our $N_z(N_z + 1)$ SINDy coefficients using the coefficients obtained on the training data Ξ and fit a GP to each SINDy parameter. We then evaluate the GPs to interpolate SINDy coefficients for a new, unseen parameter value.

Specifically, given an input parameter $\boldsymbol{\mu}^{(*)}$, we want to obtain a SINDy coefficient $\Xi_{j,k}^{(*)}$. To this end, we define $X \in \mathbb{R}^{N_\mu \times N}$ to be a matrix whose rows are the input training parameters, and $\mathbf{y} \in \mathbb{R}^{N_\mu}$ to be the values of the SINDy coefficient for each training parameter

$$X = [\boldsymbol{\mu}^{(0)}, \dots, \boldsymbol{\mu}^{(N_\mu)}]^\top, \quad \mathbf{y} = [\Xi_{j,k}^{(0)}, \dots, \Xi_{j,k}^{(N_\mu)}]^\top. \quad (13)$$

We also choose a kernel k with parameters $\boldsymbol{\theta}_{\text{gp}}$, such as a radial basis function

$$k(\mathbf{x}, \mathbf{x}') = A \exp\left(-\frac{1}{2} \frac{\|\mathbf{x} - \mathbf{x}'\|^2}{L^2}\right), \quad \boldsymbol{\theta}_{\text{GP}} = (A, L), \quad (14)$$

where A and L are constants which are optimized to maximize the marginal likelihood $p(\mathbf{y}|X)$. We define the vector $\mathbf{k}^{(*)}(\boldsymbol{\mu}^{(*)}, X) \in \mathbb{R}^{N_\mu}$ and matrix $K(X, X) \in \mathbb{R}^{N_\mu \times N_\mu}$ with entries given by

$$\left[\mathbf{k}^{(*)}(\boldsymbol{\mu}^{(*)}, X)\right]_i = k(\boldsymbol{\mu}^{(*)}, \boldsymbol{\mu}^{(i)} | \boldsymbol{\theta}_{\text{gp}}), \quad \left[K(X, X)\right]_{i,j} = k(\boldsymbol{\mu}^{(i)}, \boldsymbol{\mu}^{(j)} | \boldsymbol{\theta}_{\text{gp}}). \quad (15)$$

As in [6], the predictive mean and variance for a SINDy coefficient are then given by

$$m_{j,k}^{(*)} = \mathbf{k}^{(*)}(\boldsymbol{\mu}^{(*)}, X)^\top (K(X, X) + \sigma^2 I_{N_\mu})^{-1} \mathbf{y} \quad (16)$$

$$(s_{j,k}^{(*)})^2 = k(\boldsymbol{\mu}^{(*)}, \boldsymbol{\mu}^{(*)}) - \mathbf{k}^{(*)}(\boldsymbol{\mu}^{(*)}, X)^\top (K(X, X) + \sigma^2 I_{N_\mu})^{-1} \mathbf{k}^{(*)}(\boldsymbol{\mu}^{(*)}, X). \quad (17)$$

Repeating this process for every coefficient $\Xi_{j,k}^{(*)}$, we obtain a mean $m_{j,k}^{(*)}$ and standard deviation $s_{j,k}^{(*)}$ for each SINDy coefficient. When predicting for a test parameter $\boldsymbol{\mu}^{(*)}$, we have two choices evolving the compressed initial condition. Our first choice is to evolve in the latent space using the mean SINDy coefficients provided by the GPs. However, we can also sample the GPs for each SINDy coefficient several times to get multiple predictions for latent space dynamics. Decoding these predictions provides a different reconstructions of the state vector for each sample. Calculating the variance of these predictions, we obtain a measure of uncertainty for GPLaSDI without any knowledge of the governing equations. We will show in Section 5 that this uncertainty is helpful as an a priori measure of how accurately mLaSDI will predict on the test data.

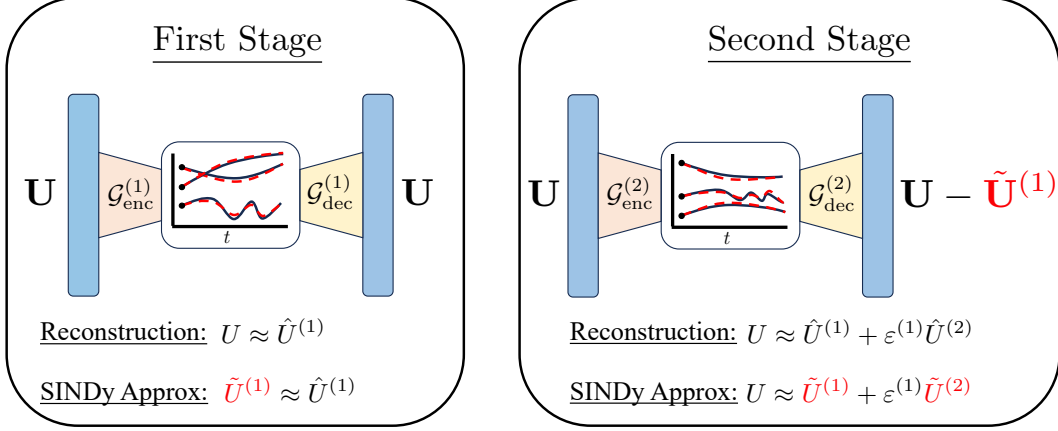


Figure 1: Schematic of mLaSDI. The first stage learns an autoencoder that reconstructs data and identifies latent dynamics using SINDy (dashed red lines). The second stage takes the training data as input and maps to residual error from the first stage. The second stage also learns an entirely new latent space representation and set of SINDy coefficients.

3 mLaSDI

Training with loss function (12) means that our autoencoders attempt to learn latent space trajectories which satisfy linear ODEs while also reconstructing the training data. Hence, the representations our autoencoders can learn in the latent space are heavily restricted compared to networks trained without any form of dynamics identification. As we will show in Section 4, placing these restrictions on the autoencoder may inhibit us from learning accurate representations of the training data, especially for complex or high-frequency signals.

This is the primary motivation behind introducing multi-stage Latent Space Dynamics Identification. Using multiple autoencoders, we are able to improve prediction errors and reduce training time compared to using a single autoencoder. This also allows us to perform less hyperparameter searching, as we are able to implement multiple smaller autoencoders to achieve high accuracy. Figure 1 provides a diagram explaining mLaSDI.

The first stage of mLaSDI is identical to the GPLaSDI algorithm as described in Section 2. For training data \mathbf{U} , we obtain the autoencoder reconstruction of the data from the first stage $\hat{\mathbf{U}}^{(1)}$, where here the superscript refers to the fact that this is the first stage, rather than the parameter value. We also have SINDy coefficients which correspond to the input parameters of our training data. So, we can obtain SINDy reconstructions of the training data $\tilde{\mathbf{U}}^{(1)}$ by compressing the initial conditions and solving the ODEs associated to each of the training parameters.

After training the first stage, it may be the case that the training data is not reconstructed accurately. When this happens, we have no hope of accurately predicting the solution for unseen input parameters. With the goal of improving our reconstructions, we consider the residual between the true training data $\mathbf{U}^{(1)}$ and the SINDy reconstructions of the training data $\tilde{\mathbf{U}}^{(1)}$

$$\mathbf{R}^{(1)} = \mathbf{U} - \tilde{\mathbf{U}}^{(1)}. \quad (18)$$

For mLaSDI, we introduce a second autoencoder which takes the training data as input, and attempts to reconstruct the (normalized) residual (18). More precisely, we introduce mappings for the second stage $\mathcal{G}_{\text{enc}}^{(2)} : \mathbb{R}^{N_u} \rightarrow \mathbb{R}^{N_z}$, $\mathcal{G}_{\text{dec}}^{(2)} : \mathbb{R}^{N_z} \rightarrow \mathbb{R}^{N_u}$. The second autoencoder learns mappings which attempt to minimize

$$\mathcal{L}_{\text{AE}}^{(2)}(\boldsymbol{\theta}_{\text{enc}}^{(2)}, \boldsymbol{\theta}_{\text{dec}}^{(2)}) = \|\varepsilon^{(1)} \mathbf{R}^{(1)} - \mathcal{G}_{\text{dec}}^{(2)} \mathcal{G}_{\text{enc}}^{(2)} \mathbf{U}\|^2, \quad (19)$$

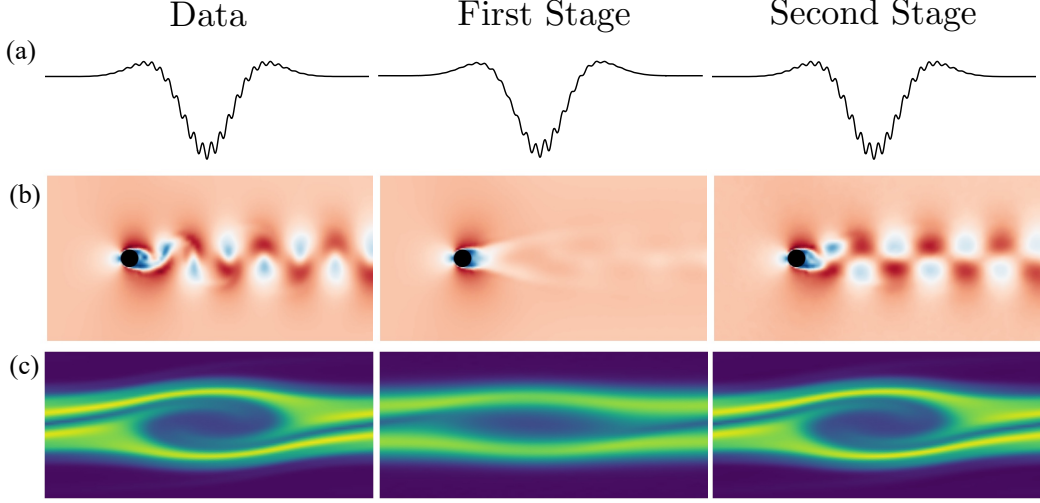


Figure 2: We apply mLaSDI to a wide range of problems including (a) our synthetic test problem (23), (b) vortex shedding, and (c) the 1D-1V equation. We show the data, and approximations from the first and second stages of mLaSDI.

where the normalization factor $\varepsilon^{(1)}$ is standard deviation of the residual calculated over all dimensions. We train the second autoencoder to learn a new set of SINDy coefficients and a new latent space representation of the data by minimizing the loss function

$$\mathcal{L}^{(2)}(\boldsymbol{\theta}_{\text{enc}}^{(2)}, \boldsymbol{\theta}_{\text{dec}}^{(2)}, \Xi^{(2)}) = \mathcal{L}_{\text{AE}}^{(2)}(\boldsymbol{\theta}_{\text{dec}}^{(2)}, \boldsymbol{\theta}_{\text{dec}}^{(2)}) + \beta_1^{(2)} \mathcal{L}_{\text{DI}}^{(2)}(\Xi^{(2)}) + \beta_2^{(2)} \|\Xi^{(2)}\|_2^2. \quad (20)$$

With this approach we can sequentially train multiple autoencoders to approximate the training data \mathbf{U} as

$$\mathbf{U} \approx \tilde{\mathbf{U}}^{(1)} + \varepsilon^{(1)} \tilde{\mathbf{U}}^{(2)} + \varepsilon^{(2)} \tilde{\mathbf{U}}^{(3)} + \dots + \varepsilon^{(n-1)} \tilde{\mathbf{U}}^{(n)}, \quad (21)$$

where $\tilde{\mathbf{U}}^{(k)}$ is the SINDy approximation of the k^{th} stage and $\varepsilon^{(k)}$ is the normalized residual

$$\varepsilon^{(k)} = \sqrt{\text{Var} \left[\mathbf{U} - \sum_{i=1}^{(k-1)} \varepsilon^{(i)} \tilde{\mathbf{U}}^{(i)} \right]}, \quad k > 0. \quad (22)$$

In practice, we will show in Section 4 that accurate results can be obtained while maintaining the same architecture between stages and increasing the SINDy weight β_1 every stage.

4 Numerical examples

mLaSDI is a general approach which we can apply to any other variant of LaSDI. Here, we focus on GPLaSDI and provide three numerical examples to demonstrate the performance of mLaSDI compared to GPLaSDI. All of our autoencoders use Tanh activation function and are trained with a fixed number of steps using Pytorch’s implementation of the ADAM optimizer [25]. GPs are fit using scikit-learn [30]. When describing network architecture we will use the notation 1000-100-10-5, which represents a fully connected network with input dimension 1000, two hidden layers (sizes 100 and 10), and output dimension 5. The decoder always has the reverse architecture of the encoder, e.g. 5-10-100-1000. In each example, we obtain training data reconstructions and test data predictions for input parameters by evolving latent dynamics using ODEs which correspond to the mean SINDy coefficients from our GPs. Full details of the hyperparameters and discretizations used are in Appendix A.

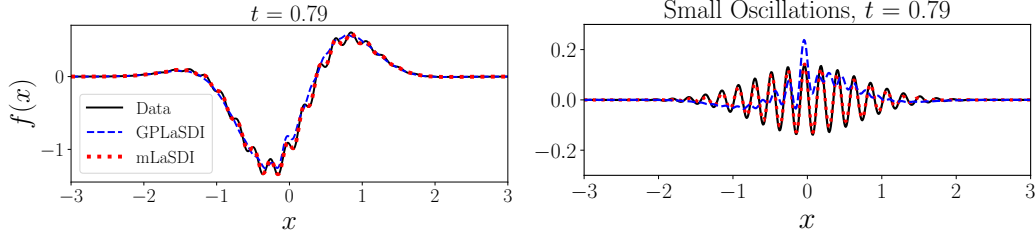


Figure 3: Applying GPLaSDI and mLaSDI with 2 stages to (23) with $A = 1.4$. (Left) Reconstruction of the training data for both methods. (Right) Results after subtracting the sine wave from the approximations to visualize how well each method approximates the small, high-frequency cosine wave. Note that the data and mLaSDI are nearly overlapping.

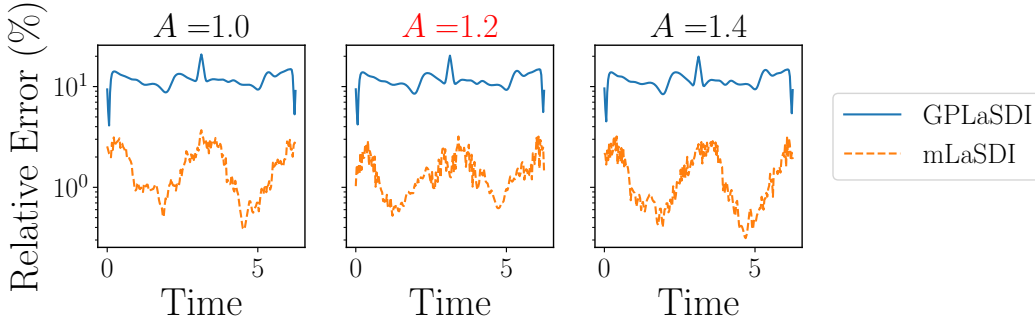


Figure 4: Relative error for GPLaSDI and mLaSDI applied to toy problem (23). GPLaSDI is trained for 50,000 iterations while mLaSDI has 2 stages each trained for 10,000 iterations. Both methods are trained on the data from cases $A = (1.0, 1.4)$, and we predict for $A = 1.2$.

4.1 Multiscale oscillating system

We begin with a proof-of-concept example to demonstrate the effectiveness of mLaSDI. Consider the highly oscillatory function

$$f(x, t; A) = A [\sin(2x - t) + 0.1 \cos((40x + 2t) \sin(t))] \exp[-x^2], \quad (23)$$

where the input parameter A controls the amplitude of the function. We generate synthetic training data from the input parameter values $A = (1.0, 1.4)$, and try to predict for the case $A = 1.2$. To demonstrate the power of our approach, we train two stages of mLaSDI for 10,000 iterations each. For comparison, we also train one stage of GPLaSDI for 50,000 iterations. Our autoencoders for both mLaSDI and GPLaSDI have the same architecture, consisting of 1 hidden layer with architecture 600-100-5.

In Figure 3 we plot a snapshot of the training data and reconstructions to show that both GPLaSDI and mLaSDI capture the behavior of the large sine wave. However, GPLaSDI struggles to capture the small cosine wave with oscillating frequency. In comparison, mLaSDI provides a significant improvement over GPLaSDI and accurately approximates both the large sine wave and small cosine wave. As we see in Figure 4, GPLaSDI's failure to capture the full behavior of the function (23) leads to training and predictive relative errors of 10–20%. mLaSDI reduces this error by an order of magnitude, achieving relative errors between 0.3–3%. We also note that GPLaSDI fails to accurately reconstruct the training data even for wider and deeper autoencoders than the one used here, shown in Appendix B.

4.2 Unsteady Wake Flow

We consider 2D unsteady wake flow, where our input parameter is the Reynolds number. We train on the velocity magnitude data for $Re = (1851.85, 3125.00)$, and try to predict evolution of velocity

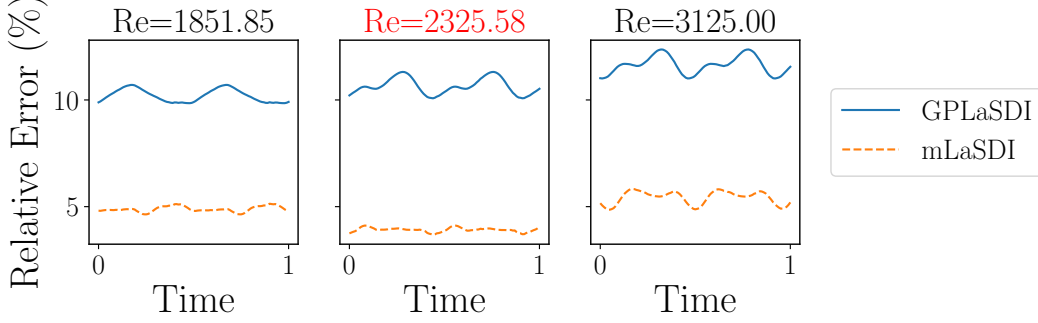


Figure 5: Relative error for GPLaSDI and mLaSDI applied to unsteady wake flow. GPLaSDI is trained for 10,000 iterations while mLaSDI has 2 stages each trained for 1,000 iterations. Both methods are trained on the data from cases $Re = (1851.85, 3125.00)$, and we predict for $Re = 2325.58$.

magnitude for $Re = 2323.58$. Similar to the previous example, we train two stages of mLaSDI for 1000 iterations each. For comparison, we also train one stage of GPLaSDI for 10,000 iterations. Our autoencoders for both methods have the same architecture, consisting of 1 hidden layer with architecture 2934-100-5.

For the training data, both GPLaSDI and the first stage of mLaSDI quickly stagnate in their learning. We refer to Figure 2(b), which demonstrates how the first stage of mLaSDI only learns the background velocity field for training data corresponding to $Re = 3125.00$. Introducing a second stage allows the new autoencoder to capture the vortex shedding, achieving relative errors below 6% on both training data and our predictive case, as shown in Figure 5. GPLaSDI exhibits similar performance as the first stage of mLaSDI, and is unable to capture more than the background field (not shown here). For this reason, GPLaSDI relative errors are greater than 10% in all cases.

4.3 Two stream plasma instability

For our final example, we examine the simplified 1D-1V Vlasov equation which describes 1D collisionless electrostatic plasma dynamics. We consider the classic benchmark two-stream instability, with initial condition

$$f(x, v, 0; \boldsymbol{\mu}) = \frac{8}{\sqrt{2\pi T}} \left[1 + 0.1 \cos(kx) \right] \left[\exp\left(-\frac{(v-2)^2}{2T}\right) + \exp\left(-\frac{(v+2)^2}{2T}\right) \right], \quad (24)$$

where $f(x, v)$ is the plasma distribution function which depends on space x and velocity v . The initial condition begins as two streams which merge to form a vortex (see Figure 2 (c)). Here, our input parameter is $\boldsymbol{\mu} = [T, k]$ with domain $\boldsymbol{\mu} \in [0.9, 1.1] \times [1.0, 1.2]$. We generate full-order model solutions for 441 parameters by discretizing the parameter space at steps $\Delta T = \Delta k = 0.01$. We then take snapshots from 25 full-order model solutions on a uniform grid as training data, and attempt to predict for the other parameters. We train mLaSDI using a wide range of architectures, latent space dimensions, and training iterations, with full experiment details given in Appendix A. To evaluate our results, we define the relative error between a full-order simulation $\mathbf{u}(t; \boldsymbol{\mu}^{(*)})$ and the mLaSDI approximation $\tilde{\mathbf{u}}(t; \boldsymbol{\mu}^{(*)})$ as

$$r^{(*)} := \max_{j=0, \dots, N_t} \frac{\|\mathbf{u}(t_j; \boldsymbol{\mu}^{(*)}) - \tilde{\mathbf{u}}(t_j; \boldsymbol{\mu}^{(*)})\|}{\|\mathbf{u}(t_j; \boldsymbol{\mu}^{(*)})\|}, \quad (25)$$

where $\|\cdot\|$ is the usual Euclidean norm. We then calculate the maximum relative errors for every parameter value $\{r^{(i)}\}_{i=1}^{N_\mu}$ in our testing set. In Figure 6 we plot the maximum, 90th, and 75th percentile errors from each autoencoder along with training time. Here 90th percentile refers to the 90th percentile maximum relative error, i.e. we sort the relative errors from least to greatest and take the value corresponding to $r^{(*)} = \lceil .9N_\mu \rceil$. The reported training times for the second stage are the total training time, i.e. the time to train the first and second stages combined. Notably, training stalled in the first stage of mLaSDI for every choice of autoencoder architecture, never reducing the

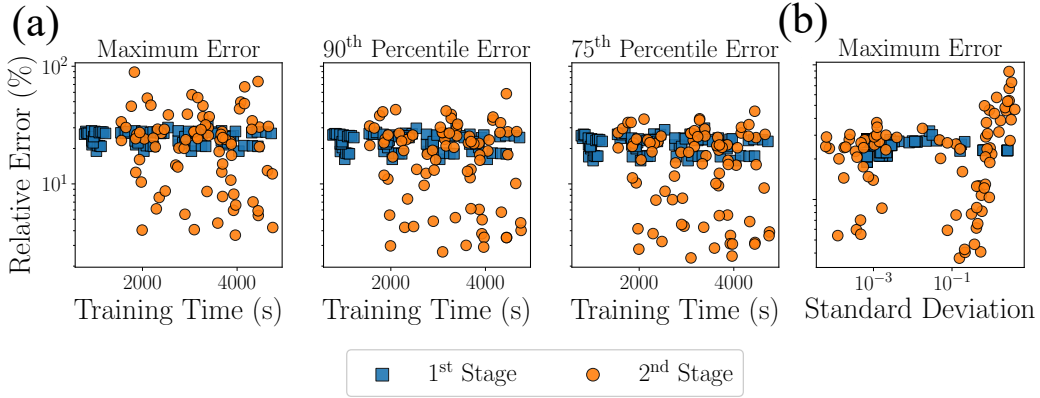


Figure 6: Applying mLaSDI with two stages to 1D-1V Vlasov equation using a wide range of architectures. (a) Percentile errors for the first and second stages using errors from (25), showing mLaSDI can offer significant reduction in error with the second stage. (b) Standard deviation of mLaSDI predictions, showing that the largest errors in the second stage coincide with highest uncertainty in the model.

relative error below even 10% relative error. By introducing the second stage, we are able to decrease maximum error to single digits with the same amount of total training time.

This experiment also reveals an important insight about mLaSDI – the second stage is not guaranteed to improve prediction accuracy. It is possible that the second stage gives similar or worse accuracy than the first stage due to high loss during training or overfitting on the training data. Fortunately, we can determine, a priori, whether second stage training is likely to be effective, without needing to run the full-order model on the test data. We discuss this in Section 5.

5 Limitations

Overfitting. One of the most significant concerns when applying mLaSDI is that autoencoders may overfit the training data, leading to poor generalization for unseen input parameters. Figure 6(a) illustrates this possibility, where some autoencoder architectures produce higher maximum relative errors in the second stage of mLaSDI than the first. By leveraging the GPs fit to the SINDy coefficients, we can estimate prediction uncertainty. Additionally, we can leverage the fact that we have a measure of prediction uncertainty from fitting GPs to our SINDy coefficients. In Figure 6(b) we plot the maximum relative error for each architecture against the prediction standard deviation when taking 50 posterior samples from the GPs. As shown in the plot, the largest maximum relative errors in the second stage coincide with the largest standard deviations. Thus, large prediction standard deviations correlate with large prediction errors, providing an a priori indicator of overfitting.

Autoencoder expressivity. At each stage of mLaSDI the autoencoder must map a latent space satisfying linear dynamics to increasingly high-frequency residuals. As stages progress, the increasing frequency of residuals makes it harder for the autoencoders to improve prediction accuracy. We see this in Figure 6, where some choices of architecture yield similar prediction accuracy across both stages. This behavior is often indicated by large latent dynamics loss during training, which signals that the autoencoder struggles to learn an effective mapping between the imposed latent dynamics and the residual. One potential approach to address this issue is increasing autoencoder width or depth in later stages as suggested in [1]. Additional hidden layers or an increased number of nodes per layer would give the autoencoders greater expressivity, improving their ability to capture high-frequency residuals in later stages.

6 Discussion

We have introduced mLaSDI as a data-driven, non-intrusive reduced-order modeling framework. mLaSDI improves both prediction accuracy and training efficiency over LaSDI variants by sequentially training multiple autoencoders, where each learns to correct the residual error of the previous one. We also reduce the need for hyperparameter tuning by instead introducing several stages. We demonstrated the efficacy of mLaSDI on a toy example, unsteady wake flow, and the 1D-1V Vlasov equation. For all examples, mLaSDI obtained accurate predictions for unseen input parameters.

Our approach provides improved prediction errors compared to LaSDI, with several promising aspects remaining to be explored. For example, integrating weak SINDy [26] rather than strong SINDy has been shown to improve results even without noisy data [17, 36]. We also believe that modifying the architecture of the autoencoders at later stages to become deeper and wider, as in [1], is a promising approach to capture high-frequency residuals at later stages. These extensions offer exciting opportunities for further advancing the mLaSDI framework.

Acknowledgments and Disclosure of Funding

This work was partially supported by the Lawrence Livermore National Laboratory (LLNL) under Project No. 50284. Livermore National Laboratory is operated by Lawrence Livermore National Security, LLC, for the U.S. Department of Energy, National Nuclear Security Administration under Contract DE-AC52-07NA27344. LLNL document release number: LLNL-CONF-2006046.

References

- [1] Z. Aldirany, R. Cottreau, M. Laforest, and S. Prudhomme. Multi-level neural networks for accurate solutions of boundary-value problems. *Computer Methods in Applied Mechanics and Engineering*, 419:116666, 2024. ISSN 0045-7825. doi: <https://doi.org/10.1016/j.cma.2023.116666>.
- [2] R. Anderson et al. Mfem: A modular finite element methods library. *Computers & Mathematics with Applications*, 81:42–74, 2021.
- [3] P. Benner, S. Gugercin, and K. Willcox. A survey of projection-based model reduction methods for parametric dynamical systems. *SIAM Review*, 57(4):483–531, 2015. doi: [10.1137/130932715](https://doi.org/10.1137/130932715).
- [4] P. Benner, P. Goyal, B. Kramer, B. Peherstorfer, and K. Willcox. Operator inference for non-intrusive model reduction of systems with non-polynomial nonlinear terms. *Computer Methods in Applied Mechanics and Engineering*, 372:113433, 2020.
- [5] G. Berkooz, P. Holmes, and J. L. Lumley. The proper orthogonal decomposition in the analysis of turbulent flows. *Annual review of fluid mechanics*, 25(1):539–575, 1993.
- [6] C. Bonneville, Y. Choi, D. Ghosh, and J.L. Belof. Gplasi: Gaussian process-based interpretable latent space dynamics identification through deep autoencoder. *Computer Methods in Applied Mechanics and Engineering*, 418:116535, 2024. ISSN 0045-7825. doi: <https://doi.org/10.1016/j.cma.2023.116535>.
- [7] C. Bonneville et al. A comprehensive review of latent space dynamics identification algorithms for intrusive and non-intrusive reduced-order-modeling. *arXiv preprint arXiv:2403.10748*, 2024.
- [8] S.L. Brunton, J.L. Proctor, and J.N. Kutz. Discovering governing equations from data by sparse identification of nonlinear dynamical systems. *Proceedings of the National Academy of Sciences*, 113(15):3932–3937, 2016. doi: [10.1073/pnas.1517384113](https://doi.org/10.1073/pnas.1517384113).
- [9] M. Calder, C. Craig, D. Culley, R. de Cani, C. A. Donnelly, R. Douglas, B. Edmonds, J. Gascoigne, N. Gilbert, C. Hargrove, F. Hinds, D. C. Lane, D. Mitchell, G. Pavey, D. Robertson, B. Rosewell, S. Sherwin, M. Walport, and A. Wilson. Computational modelling for decision-making: where, why, what, who and how. *Royal Society Open Science*, 5(6):172096, 2018. doi: [10.1098/rsos.172096](https://doi.org/10.1098/rsos.172096).

- [10] K. Champion, B. Lusch, J. N. Kutz, and S. L. Brunton. Data-driven discovery of coordinates and governing equations. *Proceedings of the National Academy of Sciences*, 116(45):22445–22451, 2019.
- [11] M. Cranmer et al. Discovering symbolic models from deep learning with inductive biases. *Advances in Neural Information Processing Systems*, 33:17429–17442, 2020.
- [12] R. M. Cummings, W. H. Mason, S. A. Morton, and D. R. McDaniel. *Applied computational aerodynamics: A modern engineering approach*, volume 53. Cambridge University Press, 2015.
- [13] A. N. Diaz, Y. Choi, and M. Heinkenschloss. A fast and accurate domain decomposition nonlinear manifold reduced order model. *Computer Methods in Applied Mechanics and Engineering*, 425:116943, 2024.
- [14] William D. Fries, Xiaolong He, and Youngsoo Choi. Lasdi: Parametric latent space dynamics identification. *Computer Methods in Applied Mechanics and Engineering*, 399:115436, 2022. ISSN 0045-7825. doi: <https://doi.org/10.1016/j.cma.2022.115436>.
- [15] C. Geuzaine and J.F. Remacle. Gmsh: A 3-d finite element mesh generator with built-in pre- and post-processing facilities. *International Journal for Numerical Methods in Engineering*, 79(11):1309–1331, 2009. doi: <https://doi.org/10.1002/nme.2579>.
- [16] X. He, Y. Choi, W.D. Fries, J.L. Belof, and J. Chen. glasdi: Parametric physics-informed greedy latent space dynamics identification. *Journal of Computational Physics*, 489:112267, 2023. ISSN 0021-9991. doi: <https://doi.org/10.1016/j.jcp.2023.112267>.
- [17] X. He, A. Tran, D.M. Bortz, and Y. Choi. Physics-informed active learning with simultaneous weak-form latent space dynamics identification. *International Journal for Numerical Methods in Engineering*, 126(1):e7634, 2025. doi: <https://doi.org/10.1002/nme.7634>.
- [18] G. E. Hinton and R. R. Salakhutdinov. Reducing the dimensionality of data with neural networks. *Science*, 313(5786):504–507, 2006.
- [19] A.A. Howard, S.H. Murphy, S.E. Ahmed, and P. Stinis. Stacked networks improve physics-informed training: Applications to neural networks and deep operator networks. *Foundations of Data Science*, 7(1):134–162, 2025. doi: 10.3934/fods.2024029.
- [20] HyPar. HyPar repository. <https://bitbucket.org/deboghosh/hypar>.
- [21] O. Issan and B. Kramer. Predicting solar wind streams from the inner-heliosphere to earth via shifted operator inference. *arXiv preprint arXiv:2203.13372*, 2022.
- [22] G.-S. Jiang and C.-W. Shu. Efficient implementation of weighted ENO schemes. *Journal of Computational Physics*, 126(1):202–228, 1996. doi: 10.1006/jcph.1996.0130.
- [23] D. Jones, C. Snider, A. Nassehi, J. Yon, and B. Hicks. Characterising the digital twin: A systematic literature review. *CIRP Journal of Manufacturing Science and Technology*, 29:36–52, 2020. ISSN 1755-5817. doi: <https://doi.org/10.1016/j.cirpj.2020.02.002>.
- [24] Y. Kim, Y. Choi, D. Widemann, and T. Zohdi. A fast and accurate physics-informed neural network reduced order model with shallow masked autoencoder. *Journal of Computational Physics*, 451:110841, 2022.
- [25] D. P. Kingma and J. Ba. Adam: A method for stochastic optimization. *arXiv preprint arXiv:1412.6980*, 2014.
- [26] D.A. Messenger and D.M. Bortz. Weak sindy: Galerkin-based data-driven model selection. *Multiscale Modeling & Simulation*, 19(3):1474–1497, 2021. doi: 10.1137/20M1343166.
- [27] D. Noble. The rise of computational biology. *Nature Reviews Molecular Cell Biology*, 3(6):459–463, 2002.
- [28] J. Sur R. Park, S.W. Cheung, Y. Choi, and Yeonjong Shin. tlasdi: Thermodynamics-informed latent space dynamics identification. *Computer Methods in Applied Mechanics and Engineering*, 429:117144, 2024. ISSN 0045-7825. doi: <https://doi.org/10.1016/j.cma.2024.117144>.
- [29] A. T. Patera, G. Rozza, et al. *Reduced basis approximation and a posteriori error estimation for parametrized partial differential equations*. 2007.
- [30] F. Pedregosa, G. Varoquaux, A. Gramfort, V. Michel, B. Thirion, O. Grisel, M. Blondel, P. Prettenhofer, R. Weiss, V. Dubourg, J. Vanderplas, A. Passos, D. Cournapeau, M. Brucher, M. Perrot, and É. Duchesnay. Scikit-learn: Machine learning in python. *J. Mach. Learn. Res.*, 12(null):2825–2830, November 2011. ISSN 1532-4435.

- [31] E. Qian, B. Kramer, B. Peherstorfer, and K. Willcox. Lift & learn: Physics-informed machine learning for large-scale nonlinear dynamical systems. *Physica D: Nonlinear Phenomena*, 406: 132401, 2020.
- [32] C. E. Rasmussen and C. K. I. Williams. *Gaussian Processes for Machine Learning*. The MIT Press, 11 2005. ISBN 9780262256834. doi: 10.7551/mitpress/3206.001.0001.
- [33] M. G. Safonov and R. Chiang. A schur method for balanced-truncation model reduction. *IEEE Transactions on Automatic Control*, 34(7):729–733, 1989.
- [34] M. Schmidt and H. Lipson. Distilling free-form natural laws from experimental data. *Science*, 324(5923):81–85, 2009.
- [35] J. Thijssen. *Computational physics*. Cambridge university press, 2007.
- [36] A. Tran, X. He, D. A. Messenger, Y. Choi, and D. M. Bortz. Weak-form latent space dynamics identification. *Computer Methods in Applied Mechanics and Engineering*, 427:116998, Jul 2024.
- [37] D. Vasileska, S. M. Goodnick, and G. Klimeck. *Computational Electronics: semiclassical and quantum device modeling and simulation*. CRC press, 2017.
- [38] P. Vincent, H. Larochelle, I. Lajoie, Y. Bengio, and P. Manzagol. Stacked denoising autoencoders: Learning useful representations in a deep network with a local denoising criterion. *Journal of Machine Learning Research*, 11(110):3371–3408, 2010.
- [39] Y. Wang and C. Lai. Multi-stage neural networks: Function approximator of machine precision. *Journal of Computational Physics*, 504:112865, 2024. ISSN 0021-9991. doi: <https://doi.org/10.1016/j.jcp.2024.112865>.
- [40] Yang Yu, Yong Ma, Xiaoguang Mei, Fan Fan, Jun Huang, and Hao Li. Multi-stage convolutional autoencoder network for hyperspectral unmixing. *International Journal of Applied Earth Observation and Geoinformation*, 113:102981, 2022. ISSN 1569-8432. doi: <https://doi.org/10.1016/j.jag.2022.102981>.
- [41] J. Zabalza, J. Ren, J. Zheng, H. Zhao, C. Qing, Z. Yang, P. Du, and S. Marshall. Novel segmented stacked autoencoder for effective dimensionality reduction and feature extraction in hyperspectral imaging. *Neurocomputing*, 185:1–10, 2016. ISSN 0925-2312. doi: <https://doi.org/10.1016/j.neucom.2015.11.044>.

Table 1: Hyperparameters and training time of autoencoders for multiscale oscillating example in Section 4.1, using Tanh activation function.

Toy Problem	Training Iterations	Learning Rate	β_1	β_2	Architecture	Training Time
GPLaSDI	50,000	10^{-3}	10^{-1}	10^{-3}	600-100-5	169.11s
mLaSDI (1 st stage)	10,000	10^{-3}	10^{-1}	10^{-3}	600-100-5	35.63s
mLaSDI (2 nd stage)	10,000	10^{-3}	10^0	10^{-3}	600-100-5	34.87s

A Experiment Details

In this section we provide full experiment details, including methods for data generation and training of our autoencoders.

For all examples in the manuscript, our autoencoders were trained using the PyTorch implementation of the Adam optimizer [25] with Tanh activation function. We provide hyperparameters for each neural network in the sections below.

When optimizing the GP parameters for our SINDy coefficients, we use the GaussianProcessRegressor from scikit-learn [30]. We use the Matérn kernel

$$k(\mathbf{x}, \mathbf{y}) = \frac{1}{\Gamma(\nu)2^{\nu-1}} \left(\frac{\sqrt{2\nu}}{l} \|\mathbf{x} - \mathbf{y}\|^2 \right)^\nu K_\nu \left(\frac{\sqrt{2\nu}}{l} \|\mathbf{x} - \mathbf{y}\|^2 \right), \quad (26)$$

where $\Gamma(\cdot)$ is the Gamma function, K_ν is a modified Bessel function, and we set $\nu = 1.5$. We now describe hyperparameters and data generation for each experiment.

A.1 Multiscale oscillating system

To generate data for this toy problem, we sample the multiscale oscillating function (23) at 201 time steps evenly distributed on the interval $[0, 2\pi]$, and 600 spatial steps evenly distributed in the interval $[-3, 3]$. This gives us 201 snapshots of each state vector $\mathbf{u}(t; A) \in \mathbb{R}^{600}$ for $A = (1.0, 1.2, 1.4)$. We train mLaSDI and GPLaSDI on the snapshots generated for $A = (1.0, 1.4)$, and predict for $A = 1.2$

Autoencoders for this toy problem were trained on CPU using a 2021 MacBook Pro with Apple M1 Max Chip and 32 GB of memory. Table 1 contains all hyperparameters for the training of GPLaSDI and mLaSDI.

A.2 Unsteady Wake Flow

For unsteady wake flow, we solve the incompressible Navier–Stokes equations

$$\frac{\partial \mathbf{u}}{\partial t} + (\mathbf{u} \cdot \nabla) \mathbf{u} = -\nabla p + \frac{1}{\text{Re}} \nabla^2 \mathbf{u} \quad \text{in } \Omega \quad (27)$$

$$\nabla \cdot \mathbf{u} = 0 \quad \text{in } \Omega, \quad (28)$$

where $\mathbf{u}(x, y, t) = (u_1(x, y, t), u_2(x, y, t))$ is the fluid velocity, p is the pressure, Re is the Reynolds number, and Ω is the spatial domain. We consider a 2D rectangular spatial domain given by $x = [0, 1]$, $y = [0, 2]$, with a cylinder of radius 0.05 centered at $(x, y) = (0.5, 0.5)$. We impose Dirichlet boundary condition at the inlet $\mathbf{u}(x, 0, t) = (0, 1)$. We apply homogeneous Dirichlet boundary conditions on the cylinder, and natural boundary conditions on the remaining boundaries.

In Figure 7 we display our mesh, which was generated using GMSH [15] and has 2,934 spatial nodes. We solve the incompressible Navier–Stokes equations using the finite element library PyMFEM’s Navier solver [2], with order 1 elements and timestep $\Delta t = 0.001$. We also refine the mesh in space once using PyMFEM, which results in 11,492 total spatial nodes. To generate data, we first run each simulation for 10 time units to ensure that vortex shedding occurs. Then, we solve for 1 additional time unit to generate 1001 time snapshots. After generating the data, we downsample in space back to our original mesh, and also only consider snapshots at every 10 timesteps. This gives us 101 snapshots of each state vector $\mathbf{u}(t; \text{Re}) \in \mathbb{R}^{2,934}$ for $\text{Re} = (1851.85, 2323.58, 3125.00)$. We train

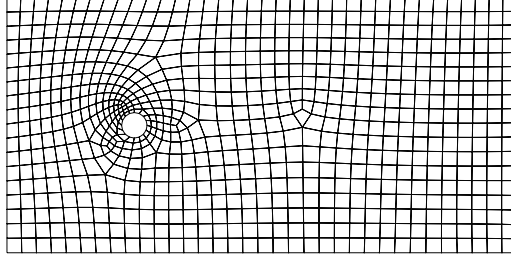


Figure 7: Mesh used to solve unsteady wake flow, rotated 90 degrees clockwise.

Table 2: Hyperparameters and training time of autoencoders for unsteady wake flow example in Section 4.2, using Tanh activation function.

Wake Flow	Training Iterations	Learning Rate	β_1	β_2	Architecture	Training Time
GPLaSDI	10,000	10^{-4}	10^{-1}	10^{-3}	2934-100-5	47.28s
mLaSDI (1 st stage)	1,000	10^{-4}	10^{-1}	10^{-3}	2934-100-5	6.45s
mLaSDI (2 nd stage)	1,000	10^{-4}	10^0	10^{-3}	2934-100-5	7.08s

mLaSDI and GPLaSDI on the snapshots generated for $Re = (1851.85, 3125.00)$ and predict for $Re = 2323.58$

Autoencoders for unsteady wake flow were trained on CPU using a 2021 MacBook Pro with Apple M1 Max Chip and 32 GB of memory. Table 2 contains all hyperparameters for the training of GPLaSDI and mLaSDI.

A.3 1D-1V Vlasov equation

For our final example, we consider the 1D-1V Vlasov equation

$$\begin{cases} \frac{\partial f}{\partial t} + \frac{\partial v f}{\partial x} + \frac{\partial}{\partial v} \left(\frac{d\Phi}{dx} f \right) = 0, & t \in (0, 5], x \in [0, 2\pi], v \in [-7, 7] \\ \frac{d^2 \Phi}{dx^2} = \int_v f dv, \\ f(x, v, 0; \boldsymbol{\mu}) = \frac{8}{\sqrt{2\pi T}} \left[1 + 0.1 \cos(kx) \right] \left[\exp \left(-\frac{(v-2)^2}{2T} \right) + \exp \left(-\frac{(v+2)^2}{2T} \right) \right]. \end{cases} \quad (29)$$

Here, $f(x, v, t)$ is the plasma distribution function which depends on space x and velocity v . The function $\Phi(x)$ is the electrostatic potential. Our initial condition consists of two streams centered at $v = \pm 2$, and is parameterized by $\boldsymbol{\mu} = [T, k]^\top$. These parameters control the width and periodicity of the two initial streams.

We solve the 1D-1V Vlasov equation using HyPar [20] with a WENO spatial discretization scheme [22] and RK4 time integration scheme with timestep $\Delta t = 0.005$. We run full-order simulations for parameter values $T \in [0.9, 1.1]$ and $k \in [1.0, 1.2]$, where the parameter ranges are discretized by $\Delta T = \Delta k = 0.01$. To generate data, we sample the solution at every timestep from a uniform 64×64 grid in the space-velocity field to obtain 251 snapshots of our state vectors $\mathbf{u}(t; \boldsymbol{\mu}) \in \mathbb{R}^{4096}$. Figure 8 displays relative errors of mLaSDI in the entire parameter space for one choice of architecture, illustrating the performance on both training and test parameters. We see how the second stage significantly increases accuracy over the first stage, sometimes by over 20%.

Autoencoders for the 1D-1V Vlasov equation were each trained on a NVIDIA V100 (Volta) GPU from the Livermore Computing Lassen system at the Lawrence Livermore National Laboratory. Table 3 summarizes all architectures used in our experiments when applying mLaSDI, and Table 4 summarizes the hyperparameters for the first and second stages of mLaSDI. In total we evaluate 80 different autoencoders for both the first and second stages.

Table 3: Autoencoder architectures used to train mLaSDI for 1D-1V Vlasov experiments in Section 4.3.

Component	Choices	Description
Hidden Layers	50, 500, 1000, 500-50, 1000-500-50	Fully connected layers
Latent Dimension	4, 5, 6, 7	Bottleneck dimension
Stage 1 Iterations	25k, 50k, 75k, 100k	Training checkpoints for first stage
Stage 2 Configurations	(25k, 25k), (25k, 50k), (50k, 50k), (75k, 25k)	(Stage 1 iter., Stage 2 iter.) pairs

Table 4: Hyperparameters of autoencoders for 1D-1V Vlasov equation example in Section 4.3, using Tanh activation function.

Vlasov	Learning Rate	β_1	β_2
mLaSDI (1 st stage)	10^{-3}	10^{-1}	10^{-3}
mLaSDI (2 nd stage)	10^{-3}	10^0	10^{-3}

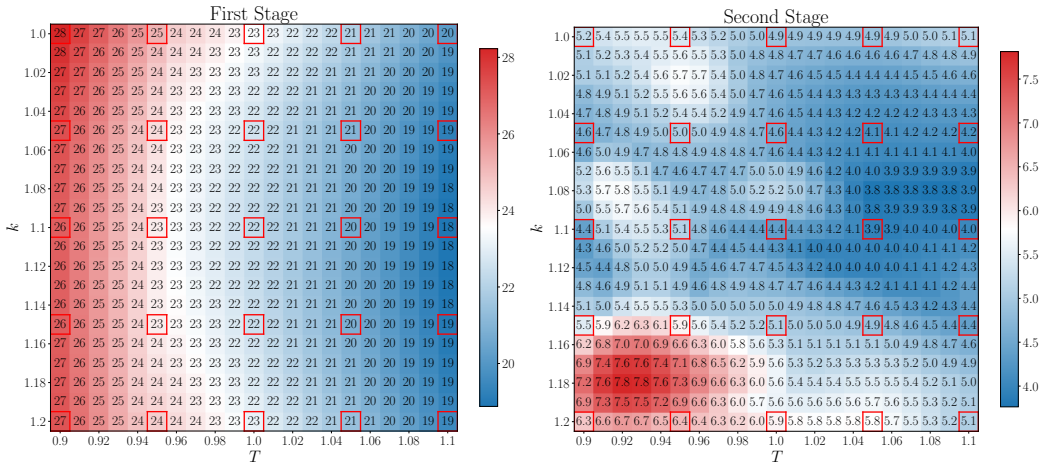


Figure 8: Relative errors applying mLaSDI with 2 stages to the 1D-1V Vlasov equation with Tanh activation function, and architecture 4096-500-50-5. The parameter values with red squares are the training parameters, and all other parameters are predictions.

B Exploring different architectures

Our numerical examples in the manuscript demonstrate that mLaSDI significantly improves prediction accuracy over GPLaSDI. To further our understanding of mLaSDI, we investigate different network architectures and activation functions. Specifically, we examine mLaSDI prediction accuracy using larger autoencoders and substituting the Tanh activation function with Softplus

$$\text{Softplus}(x) = \log(1 + e^x). \quad (30)$$

We demonstrate that the accuracy of GPLaSDI may change significantly with different activation functions, which is a key motivation for developing mLaSDI. By design mLaSDI sequentially allows us to reduce prediction errors, which minimizes the need for hyperparameter tuning and allows us to achieve high accuracy for many different autoencoder architectures.

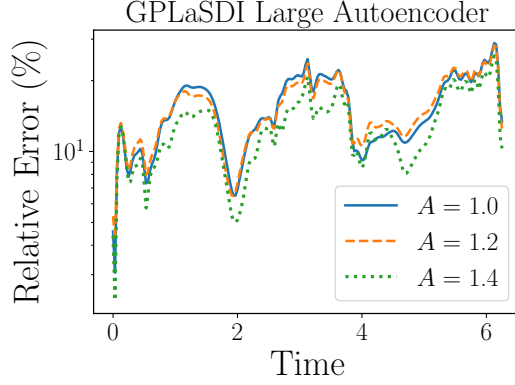


Figure 9: Relative prediction error after training GPLaSDI for 50,000 iterations and applying to toy problem (23). Here we use Tanh activation function and a larger neural network with architecture 600-250-100-50-20-10.

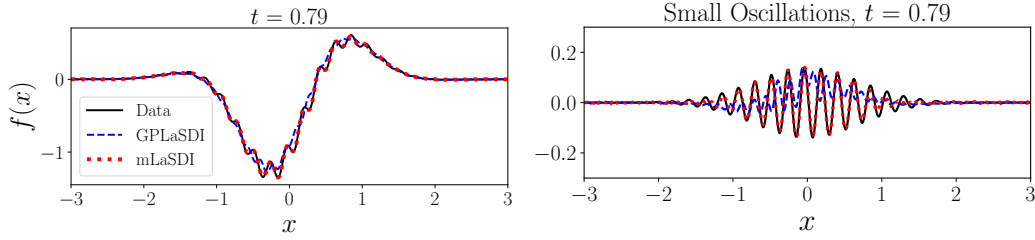


Figure 10: Applying GPLaSDI and mLaSDI with 2 stages to toy problem (23) with Softplus activation function for the case $A = 1.4$. (Left) Reconstruction of the training data for both methods. (Right) Results after subtracting the sine wave from the approximations to visualize how well each method approximates the small, high-frequency cosine wave. Note that the data and mLaSDI are nearly overlapping.

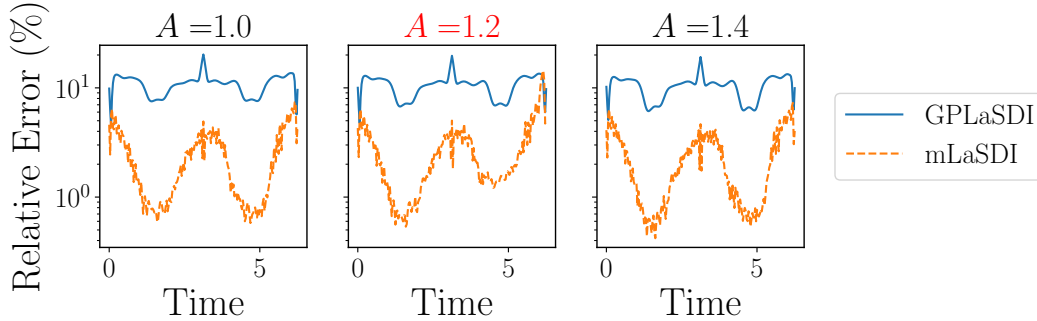


Figure 11: Relative error for GPLaSDI and mLaSDI applied to toy problem (23) with Softplus activation function. GPLaSDI is trained for 50,000 iterations while mLaSDI has 2 stages each trained for 10,000 iterations. Both methods are trained on the data from cases $A = (1.0, 1.4)$, and we predict for $A = 1.2$.

B.1 Multiscale oscillating system

Larger autoencoder. For our first experiment, we train GPLaSDI for 50,000 iterations using the same data and hyperparameters as in Section 4.1, but with a deeper autoencoder. We consider

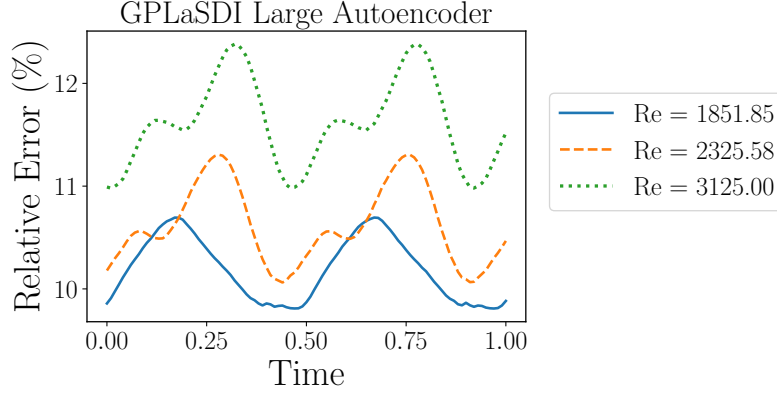


Figure 12: Relative error after training GPLaSDI for 50,000 iterations and applying to unstead wake flow. Here we use Tanh activation function and a larger neural network with architecture 2934-1000-100-50-5.

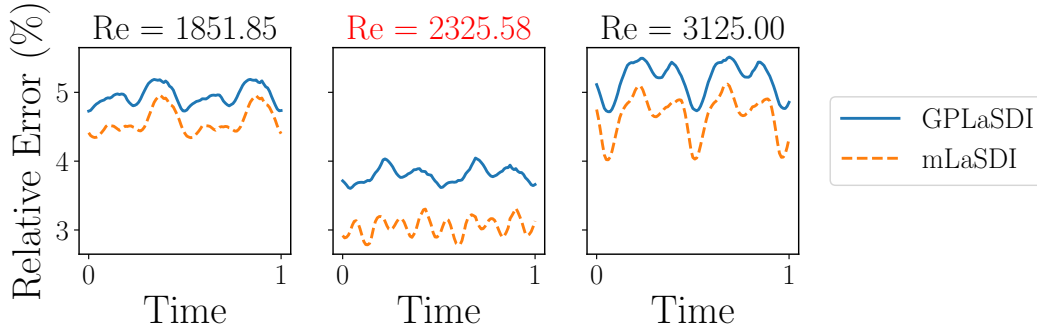


Figure 13: Relative error for GPLaSDI and mLaSDI applied to unsteady wake flow with Softplus activation function. GPLaSDI is trained for 10,000 iterations while mLaSDI has 2 stages each trained for 1,000 iterations. Both methods are trained on the data from cases $Re = (1851.85, 3125.00)$, and we predict for $Re = 2325.58$.

an autoencoder with architecture 600-250-100-50-20-10, which has 363,850 learnable parameters and took 312.92 seconds to train. In comparison, our original autoencoder for GPLaSDI had 121,805 learnable parameters and took 169.11 seconds to train. In Figure 9 we plot the relative prediction errors for this larger autoencoder, and the errors are mostly in the range of 10-30%. This is significantly larger than the errors of 0.3–3% achieved with two stages of mLaSDI, where we used smaller autoencoders which each took approximately 35 seconds to train. So, despite having a larger number of learnable parameters and taking over 4 times longer to train, mLaSDI still outperforms GPLaSDI with the larger autoencoder.

Softplus activation. For our next test we repeat the training with GPLaSDI and mLaSDI from Section 4.1, substituting Softplus activation function for Tanh in our autoencoders. The number of training iterations and hyperparameters are the same as those used in the original experiment (Table 1). In Figure 10 we plot a snapshot of the training data for $A = 1.4$ along with the approximations of both GPLaSDI and mLaSDI. Similar to the results with Tanh, GPLaSDI captures the sine wave well but is unable to capture the small high-frequency oscillations in the data. mLaSDI’s second stage allows us to accurately capture these small oscillations. This results in large relative errors for GPLaSDI, plotted in Figure 11. GPLaSDI relative errors are mostly within the range of 10–20%, while mLaSDI reduces achieves errors of 0.4–10%. We also note that in this case Softplus is less accurate than Tanh, which provided errors in the range of 0.3–3%. This will not always be the case, as we will see in our next two examples.

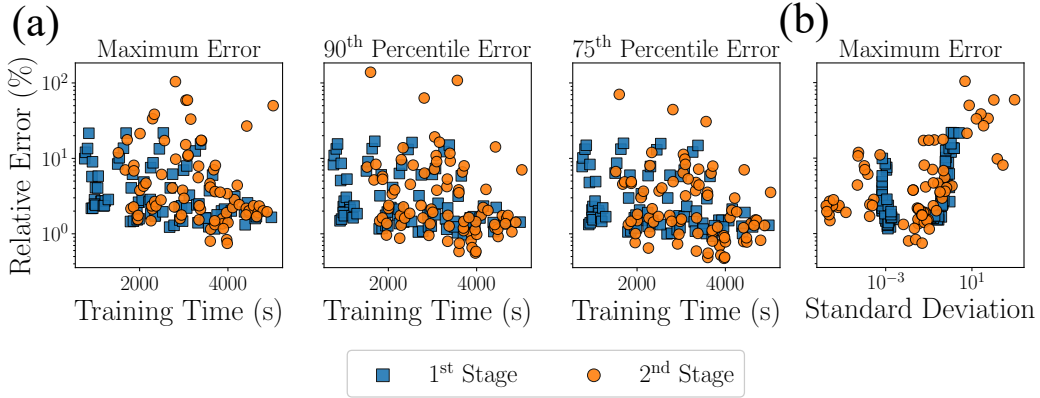


Figure 14: Applying mLaSDI with two stages to 1D-1V Vlasov equation using a wide range of architectures with Softplus activation function. (a) Percentile errors for the first and second stages using errors from (25), showing mLaSDI can offer significant reduction in error with the second stage. (b) Standard deviation of mLaSDI predictions, showing that the largest errors in the second stage coincide with highest uncertainty in the model.

C Unsteady Wake Flow

Larger autoencoder. We first train GPLaSDI for 10,000 iterations using the same data and hyperparameters as in Section 4.2, but with a deeper autoencoder. We consider an autoencoder with architecture 2934-500-250-100-50-10, which has 3,249,744 learnable parameters and took 144.10 seconds to train. In comparison, our original autoencoder for GPLaSDI had 121,805 learnable parameters and took 47.28 seconds to train. In Figure 9 we plot relative prediction errors of this larger autoencoder, and we see that they are still mostly in the range of 10–12%. This is significantly larger than the errors of 3–6% we saw with two stages of mLaSDI, using smaller autoencoders which each took 6.5–7 seconds to train. Again, mLaSDI provides significantly higher accuracy than GPLaSDI despite using a significantly smaller autoencoder and training 20 times faster.

Softplus activation. Next, we repeat the training for GPLaSDI and mLaSDI from Section 4.2, substituting Softplus activation function for Tanh in our autoencoders. The number of training iterations and hyperparameters are the same as those used in the original experiment (Table 2). When using Softplus, the first stage of GPLaSDI achieves higher accuracy compared to when using Tanh. GPLaSDI relative prediction errors with Softplus activation are within 6% for both the training and test cases. However, mLaSDI still outperforms GPLaSDI, reducing relative errors by about 0.5–1%. This small increase in accuracy reinforces the point discussed in our limitations Section 5. We are limited by autoencoder expressivity, and so we cannot always expect to gain order of magnitude accuracy increases when the first stage of mLaSDI (or GPLaSDI) performs well.

D 1D1V

Softplus activation. We repeat the same experiment on the 1D-1V Vlasov equation from Section 4.3, substituting Softplus activation function in place of Tanh. As we see in Figure 14, using Softplus significantly decreases the maximum errors when applying mLaSDI compared to Tanh for this problem. For many of the architectures, the first stage of mLaSDI performs well and gives maximum percent-errors within single digits. Nonetheless, the second stage of mLaSDI provides the lowest maximum error achieved by any of the experiments. Additionally, mLaSDI consistently provides the lowest 90th and 75th percentile errors.

Similar to the results when using Tanh, the highest maximum errors coincide with the largest uncertainty (Figure 14(b)). This reinforces our limitation that we may overfit the data, but can use

the standard deviation of predictions as an a priori indicator that the second stage results have high uncertainty and should not be trusted.

We note that Figure 14 excludes outlier results from the architectures 4096-50-5 and 4096-1000-500-50-5 because they resulted in large training losses. These results had maximum percent errors of 4,800% and 45,800% along with standard deviations of 1.5×10^{13} and 1.8×10^5 , respectively.